(Preprint) AAS 19-619

MID-LIFT-TO-DRAG RATIO RIGID VEHICLE 6-DOF EDL PERFORMANCE USING TUNABLE APOLLO POWERED GUIDANCE

Breanna Johnson,[*] Ping Lu,[†] and Christopher Cerimele[‡]

The Mid-Lift-to-Drag ratio Rigid Vehicle (MRV) is a candidate in the NASA multi-center effort to determine the most cost effective vehicle to deliver a large-mass payload to the surface of Mars for a human mission. Products of this effort include six-degree-of-freedom (6DoF) entry-to-landing trajectory performance studies for each candidate vehicle. These high fidelity analyses help determine the best guidance and control (G&C) strategies for a feasible, robust trajectory. This paper presents an analysis of the MRV's G&C design by applying common entry and descent associated uncertainties using a Fully Numerical Predictor-corrector Entry Guidance (FNPEG) and tunable Apollo powered descent guidance.

INTRODUCTION

NASA's Evolvable Mars Campaign was formulated with the goal of defining the strategy and the operational capabilities needed for a human presence further in the solar system, including Mars, starting in the 2030s. One of the great challenges is defining a feasible mission with a vehicle architecture capable of delivering a 20 metric ton (mt) payload to the surface of Mars. This requirement is based on an estimate of the minimum amount of payload required for a Mars Ascent Vehicle (MAV), which would need to be transported for a future return mission. Previous robotic missions to the Mars surface have primarily featured low ballistic entry vehicles with parachutes that deploy at subsonic velocities to ensure a soft touchdown. However, multiple sources have demonstrated that with the current state of the art technology, this approach would be infeasible for a human mission due to the large mass required and low density of the Mars atmosphere. For this reason, the Mid-Lift-to-Drag ratio Rigid Vehicle (MRV) will need to use supersonic-retro-propulsion (SRP) in its descent and landing phases of flight.

Robotic and even human missions have utilized some version of the heritage Apollo entry guidance to achieve soft touchdown and precision landing, such as the Mars Science Laboratory (MSL) and Orion vehicles.[1, 2] A human mission to Mars would require an even smaller footprint from the recent MSL landing ellipse of 25x20 km,[3] as well as experience smaller peak g-loads than the previous MSL robotic mission. Typical human safety requirements for human missions are limited to 4 g's for a deconditioned crew, while MSL experienced nominal peak loads of up to 10 g's.[1] For these reasons, the entry, descent, and landing (EDL) guidance and control (G&C) strategy for a human mission to Mars must be capable of providing soft and precision landing, while abiding human safety constraints.

[*] Aerospace Engineer, Flight Mechanics and Trajectory Design Branch NASA JSC/EG5.
[†] Professor and Chair, Department of Aerospace Engineering; plu@sdsu.edu, Fellow AIAA.
[‡] EDL Domain Lead, Aerosciences and Flight Mechanics Division, NASA JSC/EG5.

METHODOLOGY

The JSC Flight Analysis and Simulation Tool (FAST) is used to develop and simulate both the 3DoF and 6DoF EDL solution. Previous 6DoF EDL simulation results used a vehicle shape generated by the Co-Optimization Bluntbody Re-entry Analysis (COBRA) tool to optimize aerodynamic and aerothermal properties by changing the Outer Mold Line (OML) of the MRV.[4] These methods were again employed to update the vehicle properties from the CobraMRV 2908b to the CobraMRV 2908g OML. With this update, the vehicle entry mass of 58.7 mt also increased to 61.8 mt. Improvements to the design included smoothing the transition from the fuselage to the flap hinge line, in order to reduce flap heating, as well as increased fidelity in structural and aerodynamic modeling. Although there have been updates to the vehicle structure to increase fidelity and aerodynamic characteristics, Figures 1 and 2 show that the overall dimensions of the main body remain at 19.8 m in length, 8.8 m in width, and 7.3 m in height.

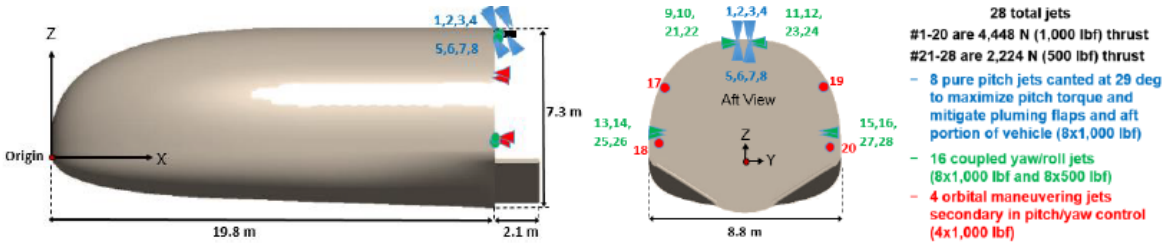

Figure 1. CobraMRV 2908b and RCS Jet Locations.

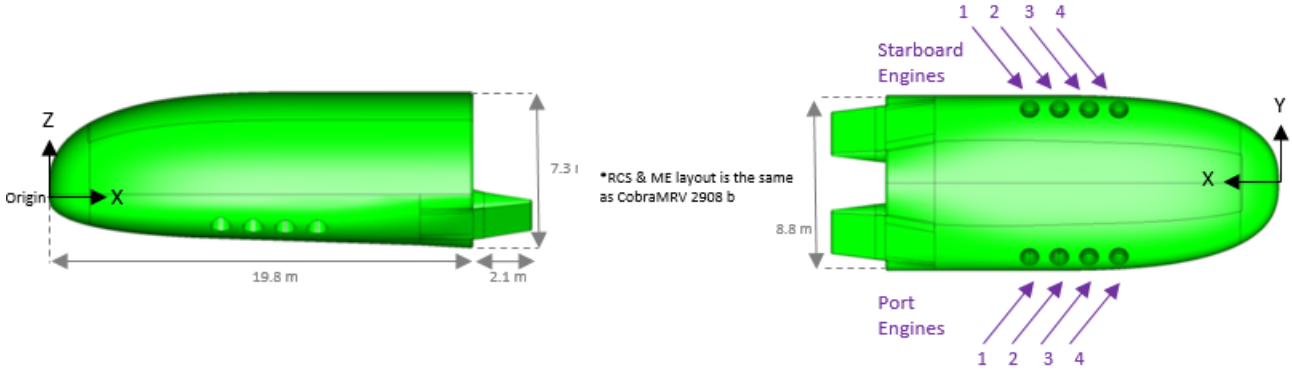

Figure 2. CobraMRV 2908g and Main Engine (ME) Jet Locations.

Similarly, the CobraMRV 2908g maintains an aerodynamic reference length of 19.8 m, a surface area of 160 m^2, a hypersonic L/D ratio of 0.54, and a ballistic coefficient of 379 kg/m^2 at entry. A total of twenty-eight 4,448 N and 2,224 N Reaction Control System (RCS) thrusters are used in conjunction with the split body flaps in order to provide trimming capabilities to reduce jet firings and bank angle modulation throughout entry. Eight 100 kN main engines are used with RCS for the descent and landing phases of flight to provide trim management and follow throttle commands.

Due to the expected ineffectiveness of the flaps with the main engines on, the RCS is used during powered descent and landing. To test that the G&C strategy is robust, vehicle candidates must meet g-load and heating constraints not only for a nominal trajectory, but must also meet these constraints even when various EDL dispersions and uncertainties are applied. Therefore a successful Monte Carlo analysis would result in maximum g-loads below 4 g's, soft landing (velocities below ~5 m/s), and a landing footprint of no more than 50m. Heating rates should be in family of what is expected for a Thermal Protection System (TPS) comprised of ablators and Shuttle derived

flexible blankets (50-60 W/cm^2).[4] This paper will assess the G&C strategy of using a Fully Numerical Predictor-corrector Entry Guidance (FNPEG) in conjunction with the newly developed Tunable Apollo Powered Descent Guidance (TAPDG)[5] to meet these constraints.

Entry Guidance and Control Overview

FNPEG, like heritage entry guidance algorithms, generates bank angle commands which serve to modulate the direction of the lift vector, such that the distance to the target is minimized and the vehicle is guided to a user-specified energy, as defined in Equation 1.[6]

$$e = \frac{1}{r} - \frac{V^2}{2} \tag{1}$$

In order to reduce stress on the RCS and save propellant, the commanded angle of attack and sideslip angles are set at the vehicle's natural aerodynamic trim stability points, based on the expected location of the center of gravity (CG). The magnitudes of the guided bank angle commands follow a linear profile with energy, as shown in Figure 3, where ϕ_0 represents the vehicle's current bank angle and normalized energy and where ϕ_f is a user defined constant defined a priori that may be tuned to improve robustness to dispersions.[7]

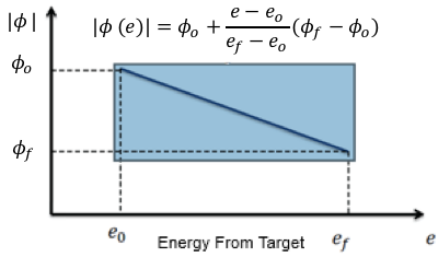

Figure 3. Linear bank angle profile with energy.

The predicted bank angle command profile shown in Figure 3 is generated based on the current state at each guidance step in addition to the solved equations of motion that are used to predict the full trajectory. If the predicted trajectory does not reach the target at the user defined energy, ϕ_0 is corrected through an iterative Gauss-Newton method solver until the range to target (s) error function, as defined in as defined in Equation 2, is minimized.[6]

$$f(\phi_0) = \frac{1}{2}\left[s(e_f) - s_f^*\right]^2 \tag{2}$$

Bank angle modulation is primarily achieved with the twenty-eight engines shown in Figure 1, while trim stability is primarily maintained with the split body flaps located at the aft of the vehicle, serving as the coupled rudder and elevon. The classical control algorithm used in entry determines the gains required based on the current estimated dynamic pressure and the desired augmented frequency in the longitudinal and lateral directional axes.[8] In order to achieve the desired system response in accordance with Equations 3 and 4, gains may be derived from Equations 5-7 in order to determine appropriate proportional and derivative gains.

$$\ddot{\alpha} + 2\xi\omega_{SP}\dot{\alpha} + \omega_{SP}^2\alpha = 0 \tag{3}$$

$$\ddot{\beta} + 2\xi\omega_{DR}\dot{\beta} + \omega_{SP}^2\beta = constant \tag{4}$$

$$\tau_x = I_x\dot{p} = C_{l_\beta}\beta\bar{q}SL + m_x\left(-K_\beta\beta - K_p p + K_p r_c cot\alpha\right) + C_{l_{\delta_a}}\delta_a\bar{q}SL \tag{5}$$

$$\tau_y = I_y\dot{q} = C_{m_\alpha}\alpha\bar{q}SL + m_y\left(K_\alpha(\alpha_c - \alpha) - K_q q\right) + C_{m_{\delta_e}}\delta_e\bar{q}SL \tag{6}$$

$$\tau_z = I_z\dot{r} = C_{n_\beta}\beta\bar{q}SL + m_z(K_r r_c - K_r r) + C_{n_{\delta_a}}\delta_a\bar{q}SL \quad (7)$$

The CobraMRV design updates also led to an update in the targeted X_{CG} (10.54 m to 10.47 m) as defined in the Figure 1 coordinate system and a reduction in flap actuation rate limits (30 deg/s to 10 deg/s). Figure 4 shows the nominal trajectories, starting at an altitude of 125 km and velocity of 4.7 km/s heading north. The relative entry flight path angle is chosen at -10.2 deg and the atmosphere is modeled with MarsGRAM 2010. The Lagrangian 85x85 gravitational field is applied.

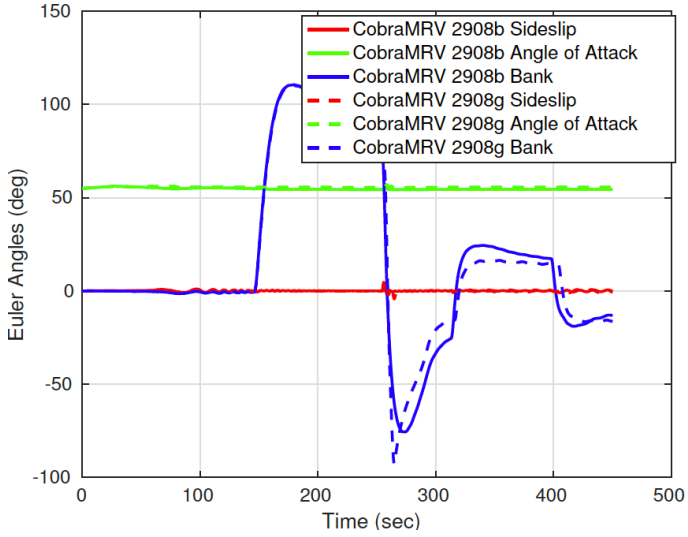

(a) Freestream to Body Euler Angles.

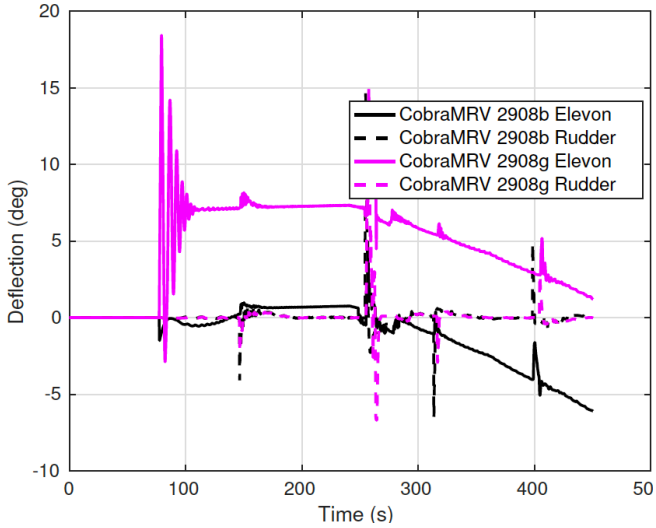

(b) *Elevon and Aileron Deflection Angles.*

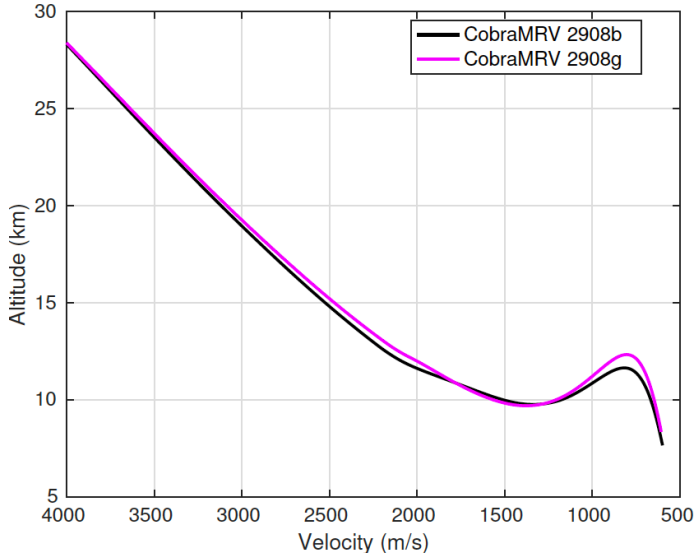

(c) Energy Profiles.

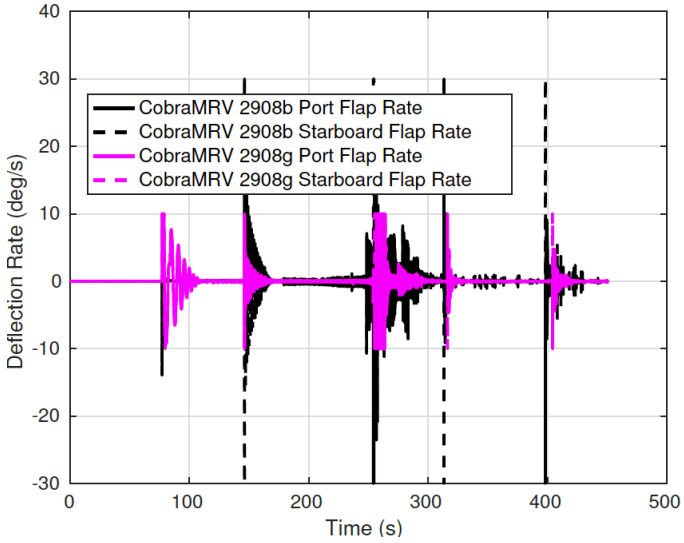

(d) *Starboard and Port Flap Rates.*

Figure 4. CobraMRV2908b and CobraMRV2908g Trajectory Comparison.

In this nominal entry trajectory, the angle of attack and sideslip angles maintain their 55 deg and 0 deg trim conditions, respectively, within their prescribed deadbands. The bank angle stays within its 1 deg deadband throughout flight and achieves the prescribed three bank reversals. And as expected, the energy and angle profiles remain to be very similar between the two CobraMRV models, as show in Figures 4a and 4c. A preliminary analysis of the flap actuator mechanism, estimated

mass properties, and power requirements was done based on similar assumptions used for the Shuttle orbiter. For this heavier vehicle, a trade study on scaling up the actuators revealed that the new left and right flap rates should not exceed 10 deg/s until further work is completed. Thus this limitation was included in the updated 6DoF simulation as shown in Figure 4d. Both CobraMRV 2908b and CobraMRV 2908g simulated trajectories yield satisfactory bank angle tracking and entry termination point targeting. The change in targeted X_{CG} from 10.54 m to 10.47 m was implemented to effectively improve yaw and pitch stability during entry. This change increases the trim nominal elevon deflection from 0 deg to 8 deg, also shown in the comparison plots of Figure 4b. Aileron trim deflection remains at 0 deg.

A CG box had been previously defined for the MRV, based on expected possible CG uncertainties that could be present at launch.[9] This box was defined as $\pm$ 20 cm in X, $\pm$ 5 cm in Y, and $\pm$ 20 cm in Z. Previous stability analyses show that for mid-L/D geometries, the vehicle is most resistant to CG uncertainty in Z and most vulnerable in Y. Additionally, there are physical limits of $\pm$35 deg deflections for the left and right flaps, which result in saturation limits of $\pm$20 deg for the elevon contribution to the aerodynamic equations and $\pm$15 deg for the rudder contribution. Figure 5a shows that if there is a maximum X_{CG} and Cm uncertainty biasing the vehicle to pitch up, the elevon would trim at a more positive value of 20 deg in order to produce a negative pitching moment to counteract the disturbance. The updated nominal X_{CG} and nominal elevon deflection of 8 deg also improved coverage of the longitudinal CG box, such that maximum elevon deflections of $\pm$ 20 deg, can sufficiently eliminate destabilizing moments from $\pm$20 cm X_{CG} offsets. In fact, designated pitch RCS jets are consistently the least active of all RCS jets, as shown in Figure 5d.

Similarly, rudder deflections of $\pm$15 deg, can help to reduce destabilizing moments from $\pm$5 cm Y_{CG} offsets. Figure 5b illustrates the vehicle response to a lateral worst case offset if Y_{CG} is moved 5 cm starboard. This worst case is also coupled maximum estimated rolling moment uncertainties. The controllability in the face of these uncertainties highlight the vehicle's robustness to the common issues that often hurt vehicles of the mid-L/D class. Due to the vehicle's asymmetry, moments induced by the CG offset from nominal in the Y direction may be naturally trimmed only with a combination of rudder deflection and non-zero sideslip angle. It is for these reasons, a sideslip angle deadband of 5 deg was chosen to allow for equilibrium to be reached even in the event of a maximum Y_{CG} offset.

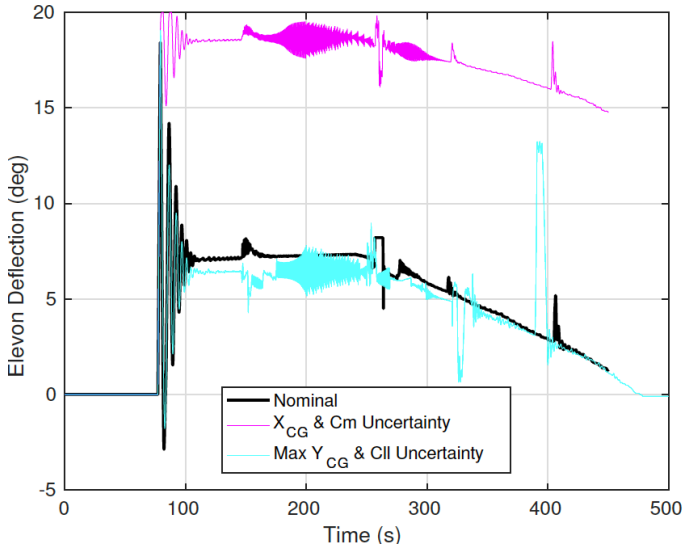

(a) Elevon Deflection vs. Time.

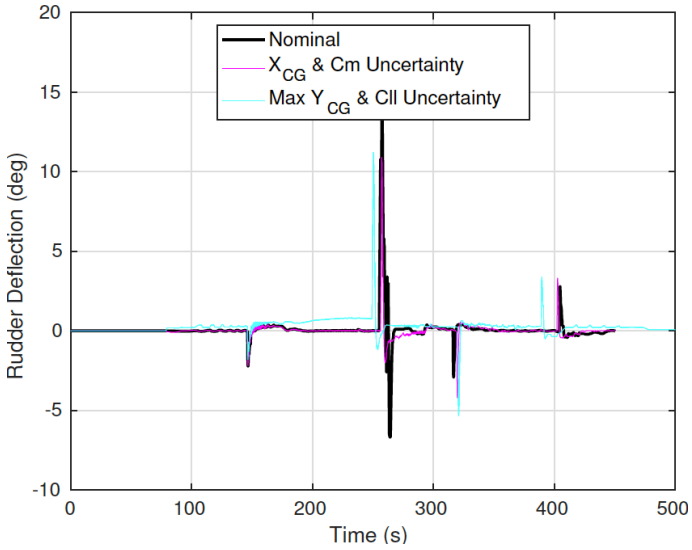

(b) Rudder Deflection vs. Time.

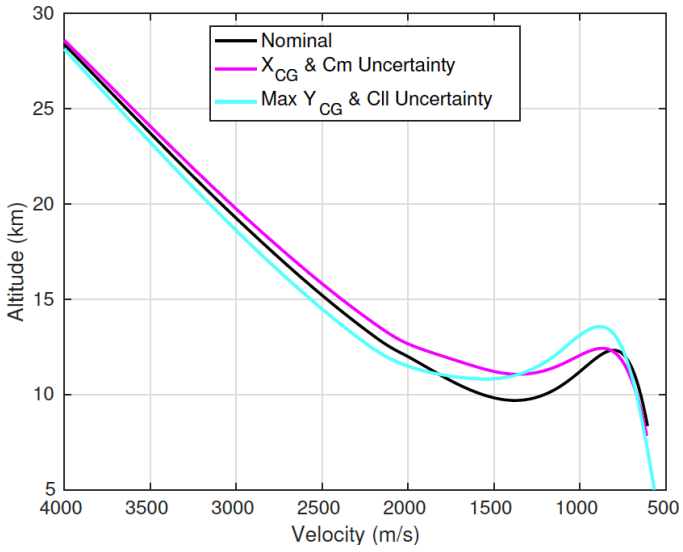

(c) Energy Profile.

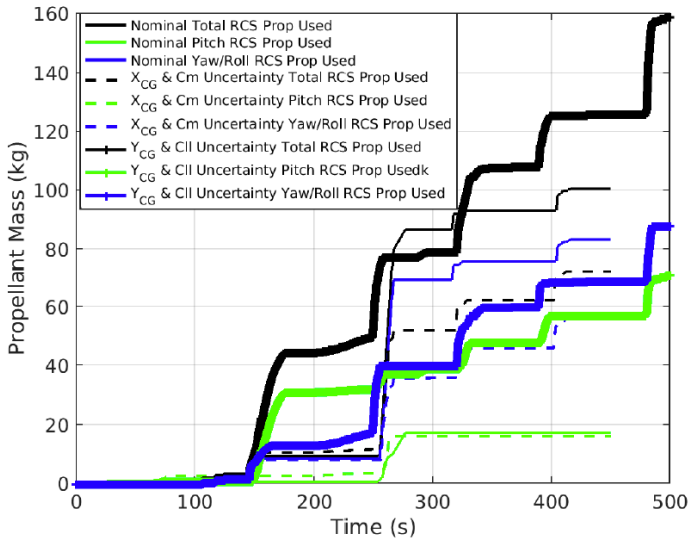

(d) Propellant Used per Axis vs. Time.

Figure 5. CobraMRV 2908g Nominal vs. Maximum Aerodynamic & CG Uncertainty Comparison.

The angle of attack deadband is tighter at 1 deg about trim due to better trim capabilities of the elevon, as compared to the rudder, and better overall static stability.[8]

Descent and Landing Gravity Turn Guidance and Control Overview

Ensuring that the descent and landing phase is as close to fuel optimal as possible is desired for a human Mars mission to reduce costs and maximize payload mass. And while global fuel optimality is desirable, realistic engine design constraints and uncertainties limit feasible optimal powered descent guidance strategies, which prompt the desire for a throttle and energy profile that can be shaped. Previous analysis shows that while an open-loop simple constant thrust gravity turn may be near propellant optimal for a nominal trajectory, it sacrifices in robustness to dispersions at engine startup and would inherit any position error from entry dispersions. Conversely, constant acceleration analytical closed-loop gravity turns have some increased robustness to dispersions to achieve soft landing, but typically require even more fuel.[9] While gravity turns allow for soft landing trajectories with simplified guidance logic, gravity turn options have shown poor performance in precision landing due to the fact that the primary objective of a gravity turn is only to achieve a soft landing. This is evidenced by a lack of a target site error penalty in the closed loop analytical gravity turn guidance law defined by Equation 8.[9]

$$\left(\frac{a_T}{g}\right)^2 + sin\,\gamma_0\,\left(\frac{V_0^2}{2h_0 g}\right)\frac{a_T}{g} - \left[\frac{V_0^2(1+\sin^2\gamma_0)}{4h_0 g} + 1\right] = 0 \qquad (8)$$

The TAPDG guidance law is an improvement from previous studies using a constant acceleration gravity turn due to its near propellant optimal solutions and flexibility.[9] While the Apollo lunar descent guidance has no free parameter to tune, the recently developed TAPDG allows the user to adjust a gain k_r to either achieve a near propellant-optimal trajectory or shape the powered descent trajectory's energy profile to improve landing conditions. The TAPDG law is given by [5]

$$\boldsymbol{a_T} = \frac{2}{t_{go}}\left(1 - \frac{1}{3}k_r\right)\left[\boldsymbol{V_f^*} - \boldsymbol{V(t)}\right] + \frac{k_r}{t_{go}^2}\left[\boldsymbol{r_f^*} - \boldsymbol{r(t)} - \boldsymbol{V(t)}t_{go}\right] + \frac{1}{6}(k_r - 6)\boldsymbol{a_{T_f}^*} + \frac{1}{6}(k_r - 12)\boldsymbol{g} \qquad (9)$$

For different values of k_r,the TAPDG law family includes both heritage Apollo lunar descent guidance and E-guidance as special cases.[5] Specifically, when the k_r gain is set to 12, the TAPDG law

becomes the familiar Apollo lunar descent guidance,[5] and the value of 6 for k_r in Equation 9 gives rise to E-guidance.[10]

Figure 6 compares the 6DoF profiles of nominal TAPDG gains. As expected, as the value of k_r decreases, max commanded thrust increases, the altitude vs. velocity profile steepens, and propellant usage decreases. All cases are able to consistently meet the TAPDG termination point of 12.5 m altitude and 2.5 m/s velocity within sub-meter accuracy. After 544 seconds, all cases enter a constant velocity gravity turn for the vertical descent phase. The thrust profiles demonstrate the non-linear nature of the TAPDG guidance compared to the more linear constant acceleration closed-loop gravity turn profile.[9] It should be noted that higher k_r gained cases are more conservative on approach to the target, achieving higher altitudes for the same velocity, but consume more propellant. TAPDG profiles also consume more propellant than a constant thrust simple gravity turn since both soft landing and precision are pursued, but save propellant compared to a constant acceleration gravity turn (12.4 mt consumed for the nominal constant acceleration gravity turn vs. 11.9 mt for the k_r=15 gained TAPDG case).[9]

While the TAPDG algorithm offers the user the ability to essentially change the energy profile of the descent trajectory and has benefits compared to some gravity turn and fuel optimal descent guidances, the user would still need to define a time-to-go (t_{go}) and range-to-go for the powered descent initiation (PDI) condition before the SRP phase begins. Typically these values are found through trial and error and are strongly tied to a reference trajectory. However, it may also be shown that best values for the PDI conditions may be found using a sweep of different input triggers.

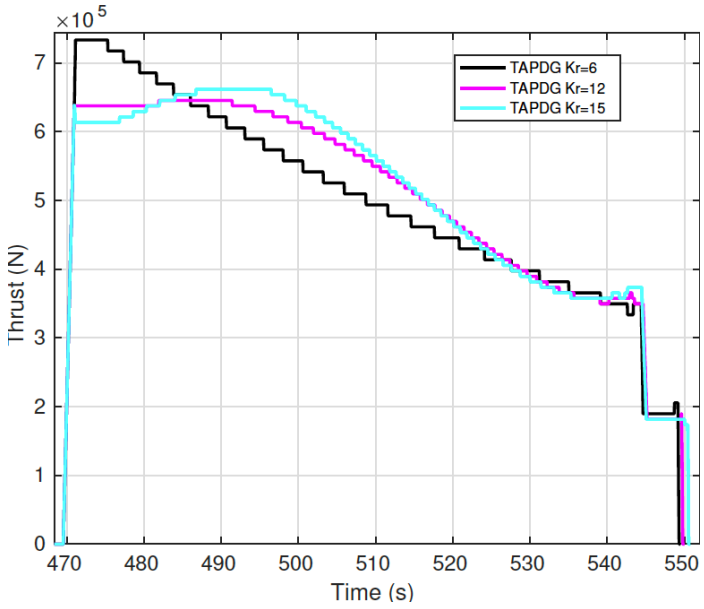

(a) Thrust Profiles TAPDG gains.

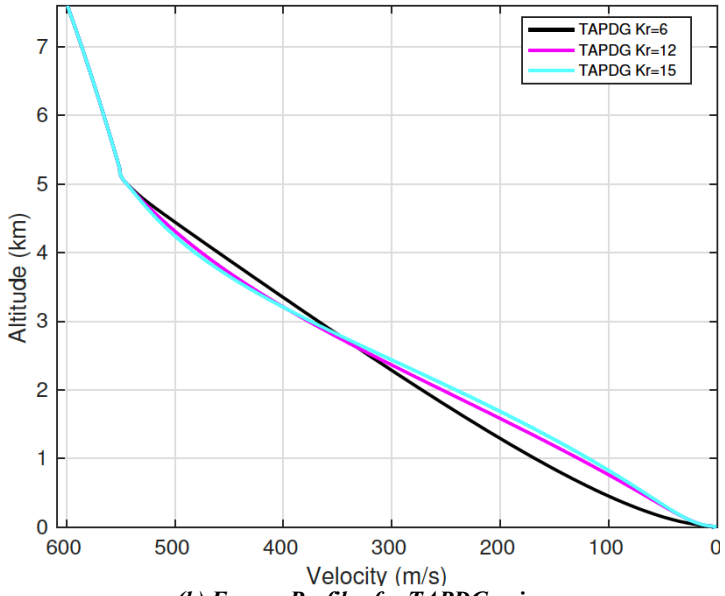

(b) Energy Profiles for TAPDG gains.

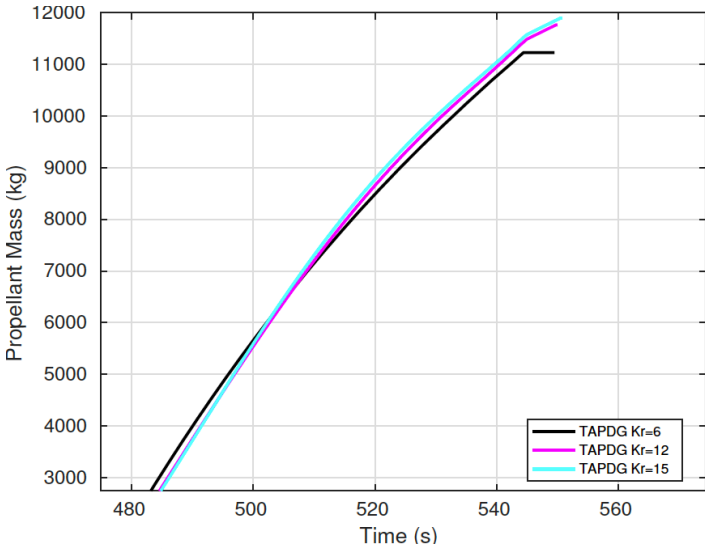

(c) Propellant Masses for TAPDG gains.

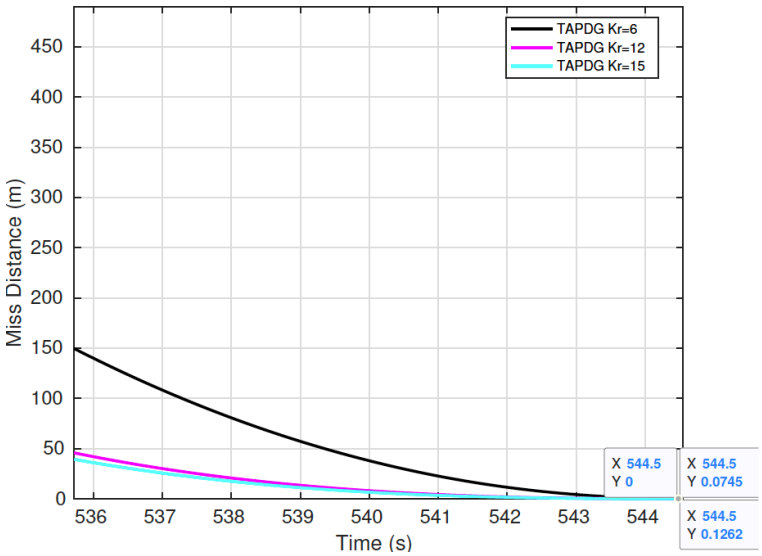

(d) Miss Distances for TAPDG gains.

Figure 6. Powered Descent Guidance Law Comparison.

Figure 7 illustrates that the likely best combination of range-to-go and time-to-go triggers until engine cutoff are between 15 and 17 km and between 70 and 80 s, due to the consistently accurate termination of entry and descent at the user specified altitude of 12.5 m and 2.5 m/s for both 3DoF and 6DoF sweeps.

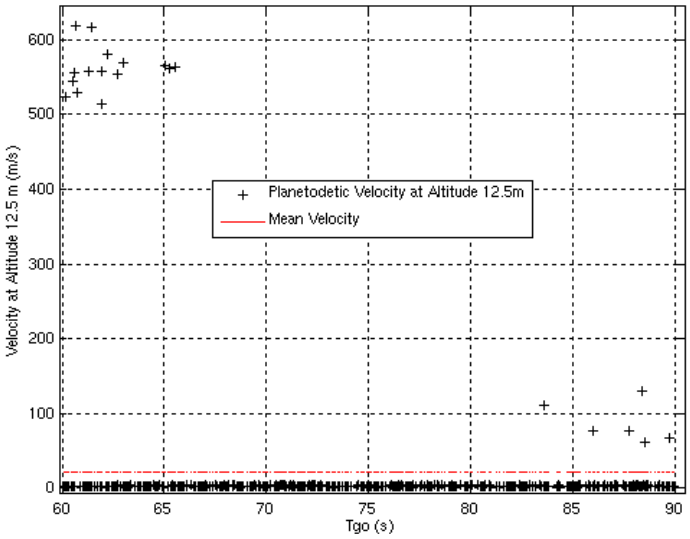

(a) Velocity at TAPDG Termination vs. Time-to-go Inputs.

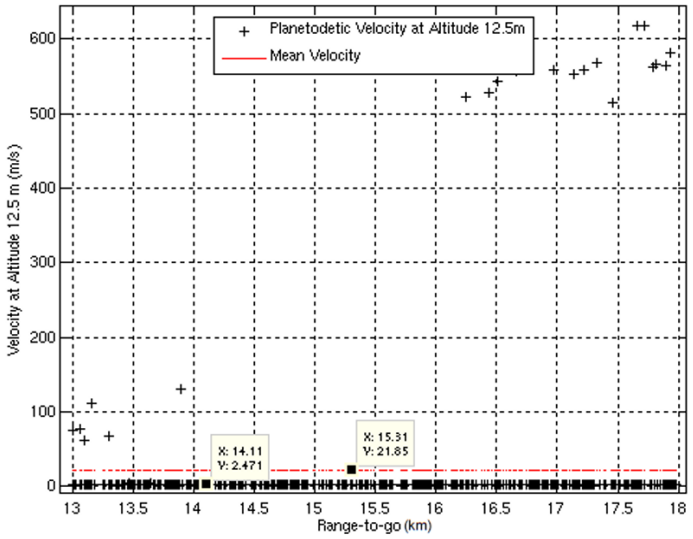

(b) Velocity at TAPDG Termination vs. Range-to-go Inputs.

Figure 7. Range-to-go and Time-to-go Sweeps for TAPDG.

Sweeps of t_{go} and range-to-go may be performed before Monte Carlo analyses to estimate the best combinations to give satisfactory results. For this study, FNPEG terminates at terminal energy targets of 2 km altitude and 350 m/s velocity and were chosen to deplete the high energy from entry as much as possible before PDI in order to reduce the needed main engine on-time. However, trade studies have shown that a specific chosen FNPEG terminal energy may not necessarily be the best

PDI condition. In fact, the most favorable PDI conditions are also highly dependent upon the powered descent guidance chosen. So TAPDG is allowed to begin once the range to go is reached, regardless of whether we have reached the FNPEG terminal energy. Once reached, FNPEG terminates and TAPDG logic continues until the desired target site and vertical descent energy is reached.

Currently, simulations for the EMC vehicle candidates have a pre-defined vertical descent phase beginning at an altitude of 12.5 m and velocity of 2.5 m/s, allowing for future navigation estimates and autonomous landing hazard and avoidance technology[8] to improve state inputs to guidance. For the MRV, the guidance law in Equation 10 is used [5]

$$\boldsymbol{a_T} = \left[\frac{\dot{h}_f^{*2} - \dot{h}^2}{2\left(h^*_f - h\right)} + g\right]\mathbf{1}_r \tag{10}$$

where $\boldsymbol{a_T}$ represents the commanded thrust acceleration vector in the direction of the planet-center position unit vector ($\mathbf{1}_r$), h and $\dot{h}$ represent the current altitude and altitude rate, h_f^* and $\dot{h}_f^*$ represent the desired altitude and altitude rate.

While navigation algorithms and their applications are not covered in this paper, including the vertical descent phase will aid in future guidance, navigation, and control robustness studies. Trajectory shaping through changing the rate of descent with respect to the groundrange before the vertical descent transition altitude, provides a powerful tool in 6DoF challenge cases, where inherent errors from entry and control rate limits impede performance. Monte Carlo results from the full end-to-end simulation in this paper will include the position errors with respect to the target at PDI to evaluate FNPEG performance, at 12.5 m altitude to assess the TAPDG performance, and at the ground to assess vertical descent and landing performance. Therefore, the trajectory shaping feature that TAPDG offers would increase the robustness to engine startup times, engine startup dispersions, throttle keep-out zones, and center of gravity uncertainties that are not typically explored with fuel optimal powered descent solutions.

MONTE CARLO RESULTS

Previous work with the MRV has shown that a hypersonic vehicle with a mid-lift-to-drag ratio (mid-L/D) can produce a nominal entry trajectory capable of meeting the human mission design derived constraints of less than 4 Earth g's and less than 5 km targeting error above the landing site.[4, 8] However, an entry-to-landing analysis of the MRV's response to dispersions would better address whether the guidance and control strategies previously presented are viable solutions to the human Mars EDL problem. For the Monte Carlo results, entry guidance is run at 1 Hz, while entry controls logic is updated at 25 Hz. Descent and landing guidance and controls logic is run at 40 Hz. The RCS provides attitude control and the eight throttleable main engines provide the desired accelerations commanded by TAPDG followed by the gravity turn guidance law in Equation 10.

Results of the Entry FNPEG Targeting Ellipse

Entry Monte Carlo dispersions include the uncertainties of aerodynamic coefficients (CA, CY, CN, Cl, Cm, and Cn), mass properties (including CG and inertia), Mars GRAM dispersions, and entry interface condition dispersions (azimuth, flight path angle, latitude, longitude, altitude). Winds are also modeled. The applied dispersions for entry are listed in Table 1.

Table 1. Entry Interface Dispersions for the Monte Carlo Simulations.

Monte Carlo Varied Parameter	Distribution	3σ / maximum	-3σ / minimum
Altitude (km)	Gaussian	1.00E-01	-1.00E-01
Longitude (deg)	Gaussian	2.50E-01	-2.50E-01
Latitude (deg)	Gaussian	2.50E-01	-2.50E-01
Velocity (m/s)	Gaussian	3.30E+00	-3.30E+00
Flight Path Angle (deg)	Gaussian	1.00E-01	-1.00E-01
Azimuth (deg)	Gaussian	1.70E-01	-1.70E-01
Mass (kg)	Gaussian	2.00E+02	-2.00E+02
Inertia (%)	Gaussian	1.00E+00	-1.00E+00
ΔX_{cg} (cm)	Uniform	2.00E+01	-2.00E+01
ΔY_{cg} (cm)	Uniform	5.00E+00	-5.00E+00
ΔZ_{cg} (cm)	Uniform	2.00E+01	-2.00E+01
CA,CN (%)	Uniform	1.00E+01	-1.00E+01
CY, Cll, Cm, Cln (deg)	Uniform	3.00E+00	-3.00E+00
Atmospheric density	Mars GRAM 2010	Mars GRAM 2010	Mars GRAM 2010
Mars GRAM 2010 dust opacity	Uniform	0.9	0.1

As the mission matures, future Monte Carlo simulations could reduce the dust opacity uncertainties to a smaller range of uncertainties based on the season that the mission is expected to fly. Due to the lack of wind tunnel testing or flight data, estimates for the kinds of aerodynamic uncertainties expected are computed and applied for Monte Carlo simulations. Estimated aerodynamic uncertainties are applied according to Equations 11 to 16, where U^m represents a multiplier applied to increase the uncertainty of an aerodynamic database and U^a represents an added uncertainty to the aerodynamic database. Note that MRC refers to the Moment Reference Center.

$$C_A = C_{A,base} + C_{A,base} * U_{C_A}^m + \Delta C_{A_{Flaps}} \quad (11)$$

$$C_Y = C_{Y,base} + U_{C_Y}^a + C_{Y_{\delta_r}} \delta_r \quad (12)$$

$$C_N = C_{N,base} + C_{N,base} * U_{C_N}^m + \Delta C_{N_{Flaps}} \quad (13)$$

$$C_{l_{CG}} = \left[C_{l,MRC} + C_Y \frac{\Delta z}{L_{ref}} + C_N \frac{\Delta y}{L_{ref}} \right] + U_{C_l}^a + C_{l_{\delta_r}} \delta_r \quad (14)$$

$$C_{m_{CG}} = \left[C_{m,MRC} + C_A \frac{\Delta z}{L_{ref}} - C_N \frac{\Delta x}{L_{ref}} \right] + U_{C_m}^a + \Delta C_{m_{Flaps}} \quad (15)$$

$$C_{n_{CG}} = \left[C_{n,MRC} - C_A \frac{\Delta y}{L_{ref}} - C_Y \frac{\Delta x}{L_{ref}} \right] + U_{C_n}^a + C_{n_{\delta_r}} \delta_r \quad (16)$$

Each aerodynamic coefficient that is zero at trim conditions is added with an estimated ± 3 deg uncertainty maximum delta from trim in sideslip or angle of attack. Thus, the bounds for these uncertainty terms in Equations 10-15 may be described by the following:

$$U_{C_A}^m = \mathrm{x} \in [-0.1, +0.1]$$

$$U_{C_Y}^a = \mathrm{x} \in [-1, +1] * U_{C_{Y,max\beta}}^a$$

$$U_{C_N}^m = \mathrm{x} \in [-0.1, +0.1]$$

$$U_{C_l}^a = \mathrm{x} \in [-1, +1] * U_{C_{l,max\beta}}^a$$

$$U_{C_m}^a = \mathrm{x} \in [-1, +1] * U_{C_{m,\max\ \alpha}}^a$$

$$U_{C_n}^a = \mathrm{x} \in [-1, +1] * U_{C_{n,max\beta}}^a$$

Each uncertainty adder's maximum value is provided in Table 1. Once better aerodynamic uncertainty values become available, the new databases will replace these estimates. However, these current uncertainties, especially when compounded by CG uncertainties, have resulted in challenge cases where trim sideslips and angles of attack are larger, and thus more conservative, compared to other flight-tested vehicles like Orion. Note that the CY uncertainty also uses an adder term, instead of the multiplier used for CA and CN, since at trim conditions, this force coefficient is zero.

While constraint enforcement on maximum g-load and heating rate is an FNPEG feature, the nominal and dispersed results did not need to enable these constraints. Although there are cases with higher g-loads that could benefit from this feature in the future. The 6DOF FNPEG entry targeting ellipse below closely matched 3DoF performance and is well within the 3-5 km ellipse targeted by MSL for parachute deployment.[1] Figure 8 shows that the latitude vs. longitude errors (miss distances) for a 1,000 case Monte Carlo resulted in all cases reaching the FNPEG terminal energy within 3 km of the target. Note that the targeting ellipse at FNPEG terminal energy (512 m/s velocity, 2.8 km altitude) is shown to highlight just FNPEG targeting, since TAPDG would actually begin at the aforementioned 17 km value of range-to-go. The targeted radius at the end of entry is less stringent than the targeted radius at the ground (50 m), as it is assumed that the powered descent and landing phase should be able to clean up errors gained during entry. It is also shown in Figure 8 that the worst case in miss distance, at approximately 3 km range error, is correlated to high rolling moment and Y_{CG} uncertainty.

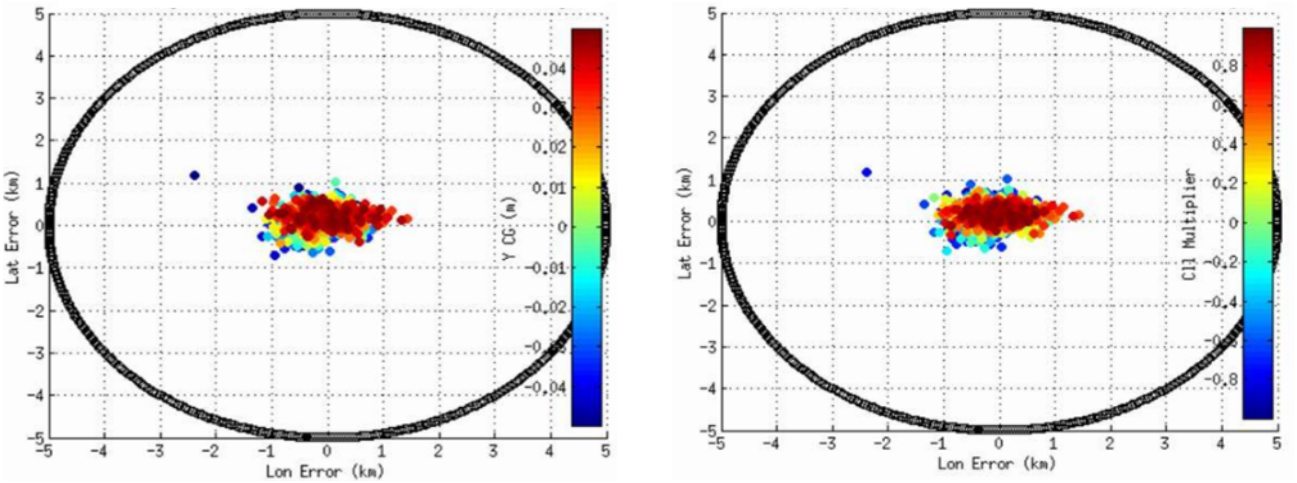

(a)Accuracy at FNPEG Terminal Energy vs. Y_{CG} Uncertainty. *(b)Accuracy at FNPEG Terminal Energy vs. Rolling Uncertainty.*

Figure 8. Miss Distance at FNPEG Terminal Energy Condition.

Before the CobraMRV 2908g update, cases like these were unable to reach the target within this radius due to the further aft X_{CG} target and weaker yaw and roll stability of the fuselage and flap system. Currently, the location of the combined fuel tanks CG is modeled as one tank and assumed coincident with the vehicle CG. RCS propellant used as well as main engine (ME) propellant used is modeled by reducing mass from this single tank.

Next, a 3,000 case end-to-end Monte Carlo was run where the FNPEG terminal energy target was 350 m/s and 2 km altitude. Since TAPDG would begin at the range-to-go of 17 km, Table 2 documents the dispersions at PDI. This Monte Carlo has a successful entry phase, as the heating remained within 50-60 W/cm^2 expectations and the g-load remained below 4 g's for the 99.75%-tile.

Table 2. Monte Carlo Simulation Results from Entry to Powered Descent Initiation.

Parameter	Mean	Standard Deviation	99.75%-tile	Minimum
Range-to-go (km)	1.70E+01	1.43E-01	1.80E+01	1.70E+01
Velocity (m/s)	5.50E+02	2.08E+01	6.20E+02	3.14E+02
Altitude (km)	4.79E+00	5.98E-01	5.65E+00	1.52E+00
Max G-load (g)	3.52E+00	2.10E-01	3.80E+00	2.56E+00
Max Heat Load (kJ/cm^2)	7.02E+00	2.39E-01	7.60E+00	6.41E+00
Max Heat Rate (W/cm^2)	5.37E+01	1.51E+00	5.80E+01	5.01E+01
Max Dynamic Pressure (kPa)	1.06E+01	9.59E-01	1.40E+01	8.18E+00
RCS Propellant Used (mt)	2.46E-01	1.33E-01	9.23E-01	3.00E-02

After satisfactory performance was observed for the 6DoF FNPEG guided entry, the next step was to test the full EDL solution to ensure that the powered descent guidance and control system could truly correct the errors in targeting from entry to land within 50m of the target.

Results of the EDL footprint

The dispersions applied for the EDL Monte Carlo case in Table 2 include those listed in Table 1 as well as powered descent associated dispersions. Each of the 8 main engines has a maximum thrust of 100 kN and maximum Isp of 360 s. Isp changes as a function of thrust, which is also modeled. The challenging increases in fidelity for powered descent include CG offset uncertainties (same as from entry), limited descent throttle rates (80 %/s), main engine startup transients (55 %/s), and main engine shutdown transients (200 %/s).[9] Uncertainties for descent and landing are given in Table 3. Each of the 8 engines are modeled with dispersions applied individually. It should be noted that the ME startup lag is a conservative estimate, but is used for this preliminary analysis until higher fidelity propulsion work is completed. Main engines are shutdown at 1 m altitude, since an engine at max thrust would need at least 0.5 s to shutdown at 200 %/s before impacting the ground. Thus, for a nominal case descending at 2.5 m/s with an engine at 80% thrust, 1 m is the minimum altitude to begin shutdown before impact. However, simulation results show that the max throttle at 1 m altitude is no more than 30% thrust, so there is margin built in here. Future work with structures and propulsion will help define the altitude vs horizontal/vertical velocity envelope at touchdown, as was done for the Apollo Lunar Module landing on the moon.[11]

Table 3. Main Engines 1-8 Dispersions for the Monte Carlo Simulation.

Monte Carlo Varied Parameter	Distribution	3σ / maximum	-3σ / minimum
ME Max Thrust (N)	Gaussian	1.00E+03	-1.00E+03
ME Throttle Rate (%)	Gaussian	1.00E+00	-1.00E+00
ME Max Isp (%)	Gaussian	1.00E+00	-1.00E+00
ME Startup Time (%)	Gaussian	1.00E+00	-1.00E+00
ME Startup Lag (s)	Gaussian	2.50E-01	0.00E+00

It should be noted that the descent and landing phases have no applied aerodynamics, as Computational Fluid Dynamics (CFD) work is ongoing for the MRV. Thus, the descent and landing phases of flight presented here should be a little more conservative in the amount of propellant needed to achieve a soft landing than if these databases were included. After scanning various t_{go} inputs, k_r gains, and range-to-go triggers, inputs of 75 s for t_{go}, 12 for k_r (Apollo), and 17 km range-to-go were first chosen for the this 6DoF EDL Monte Carlo.

Figure 9 shows that the targeted ellipse at 12.5 m altitude for the 3,000 case Monte Carlo was much smaller than the required 50 m accuracy. However there is still room for improvements, as one case was unable to meet the footprint constraints using the TAPDG inputs provided, landing at 88 m from the target for k_r=12. It was discovered that entry flap and RCS deadbands for sideslip have a large impact on number of cases that land inside the footprint. At 5 deg deadband, one extreme case with near maximum dispersions on each term in Equation 14 would never reach the desired TAPDG initiation conditions, but increasing that deadband by 20% allowed for the results shown in Tables 4 and 5, where this case does reach TAPDG initial conditions. So, there is a balance between deadbands that are too small, where the natural trim is fought by RCS, diverting resources from the bank control, and deadbands that are too large, where high allowable sideslips introduce errors in the final solution. Further investigation of this sensitivity is imperative for future work. Other important statistics about the EDL Monte Carlo performance are included in Tables 4 and 5 for 12.5 m and 0 m altitudes. From these 99.75%-tile footprint results, corresponding confidence coefficient of z_c = 3, we may conclude that if the simulation is re-run for 3,000 iterations, we are 99.75% confident that the sample mean footprint would not differ by more than 2.8% and the final velocity would not differ by more than 0.3% from the true population mean, given all the aforementioned assumptions for this simulation.[12]

While the cases are successful, the user defined t_{go} constant for TAPDG did need to be augmented with a quartic equation to estimate t_{go} in flight[13] to allow for certain challenge cases to reach the target, since the range-to-go and t_{go} inputs are sensitive to entry dispersions. Another Monte Carlo assessment will need to be performed using the Universal Powered Guidance (UPG) trigger, instead of a constant range-to-go, which would calculate the optimal PDI onboard.[6, 9] Improvements in the targeting accuracy for challenge cases have been observed in 3DoF[6] when using the UPG trigger, but will need to be tested in 6DoF to compare performance with the approach used here. Gains of k_r=6 and k_r=12 were run in Monte Carlos, but k_r=6 gave the strongest targeting accuracy for the smallest maximum propellant usage. Tables 5-7 show the results of these different gains. While there are propellant savings with k_r=6, the average miss distance increased from k_r=12 due to the fact that non-vertical components of velocity are larger at vertical descent initiation, especially with

winds. A mitigation step could be to bias the target, since the difference between the 99.75%-tile and mean are similar to k_r=12 or alter the gravity turn law in Equation 10.

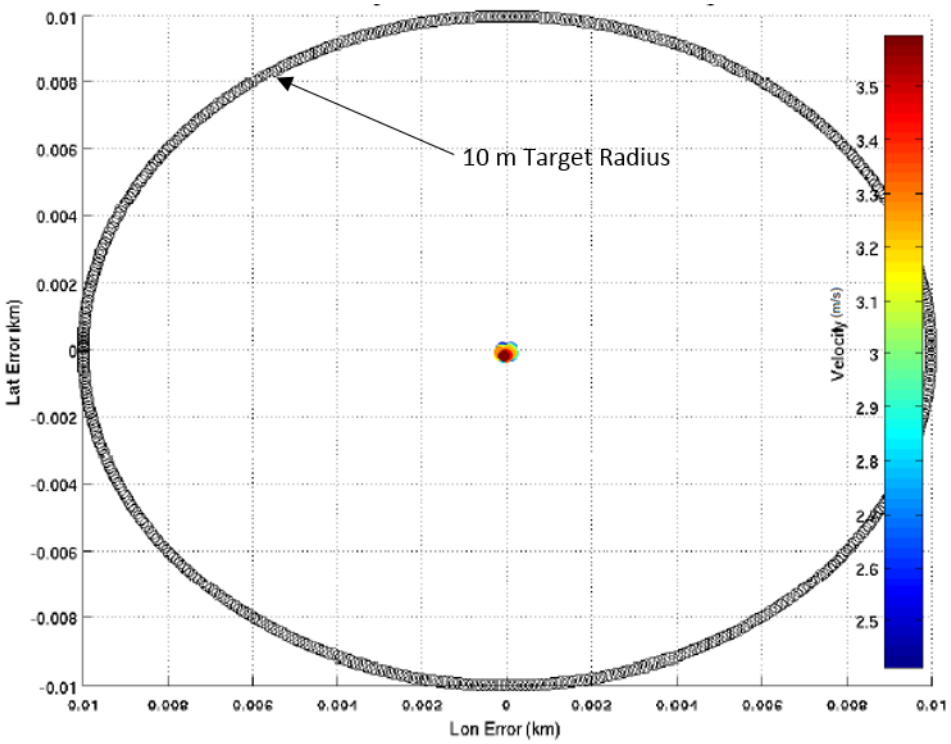

Figure 9. Miss Distance at TAPDG Target (12.5 m Altitude, k_r=12).

Table 4. Monte Carlo Results at TAPDG Target of 12.5 m Altitude (k_r=12).

Parameter	**Mean**	**Standard Deviation**	**99.75%-tile**	**Minimum**
Miss Distance (m)	1.30E-01	5.10E-02	3.32E-01	0.00E+00
Velocity (m/s)	2.87E+00	2.74E-01	3.44E+00	1.75E+00
ME Propellant Used (mt)	1.10E+01	3.40E-01	1.20E+01	9.79E+00
RCS Propellant Used (mt)	5.41E-01	1.79E-01	1.41E+00	2.50E-01

Table 5. Monte Carlo Results at Gravity Turn Target of 0.0 m Altitude (k_r=12).

Parameter	Mean	Standard Deviation	99.75%-tile	Minimum
Miss Distance (m)	4.62E+00	2.35E+00	9.54E+00	5.10E-02
Velocity (m/s)	3.65E+00	1.83E-01	5.05E+00	3.43E+00
ME Propellant Used (mt)	1.13E+01	3.33E-01	1.23E+01	1.01E+01
RCS Propellant Used (mt)	5.81E-01	1.80E-01	1.45E+00	2.82E-01
Pitch Angle (deg)	1.92E-01	6.17E-01	9.7E-01	0.00E+00

Table 6. Monte Carlo Results at Gravity Turn Target of 0.0 m Altitude (k_r=6).

Parameter	Mean	Standard Deviation	99.75%-tile	Minimum
Miss Distance (m)	1.91E+01	2.00E+00	2.51E+01	6.50E+00
Velocity (m/s)	6.98E+00	5.74E-01	9.19E+00	3.94E+00
ME Propellant Used (mt)	1.11E+01	3.10E-01	1.21E+01	9.57E+00
RCS Propellant Used (mt)	6.25E-01	1.49E-01	1.30E+00	3.20E-01
Pitch Angle (deg)	2.45E+00	8.27E-01	6.33E+00	2.78E-01

Table 7. Gain Comparison of Monte Carlo 99.75%-tile Results at 0.0 m Altitude.

Parameter	k_r=6 **99.75%-tile**	k_r=12 **99.75%-tile**
Miss Distance (m)	2.51E+01	9.54E+00
Velocity (m/s)	9.19E+00	5.05E+00
ME Propellant Used (mt)	1.21E+01	1.23E+01
RCS Propellant Used (mt)	1.30E+00	1.45E+00
Pitch Angle (deg)	6.33E+00	9.7E-01
# of cases outside 50 m radius	0	1

The next steps will be using the UPG trigger to find more aggressive trajectory profiles using less fuel with similar or better targeting accuracy. More work will also need to be done to ensure that similar accuracies can be observed once main engine aerodynamic coefficients are generated and applied to this work. Due to the complexity of the engine to engine plume interaction and high angles of attack, a CFD simulation could have a large impact on performance. Nonetheless, the

results shown in Figure 10 and Tables 5-7 certainly provide great insight into the precision and accuracy possible, even when the EDL trajectory is exposed to a multitude of expected vehicle, engine, and entry aerodynamic dispersions.

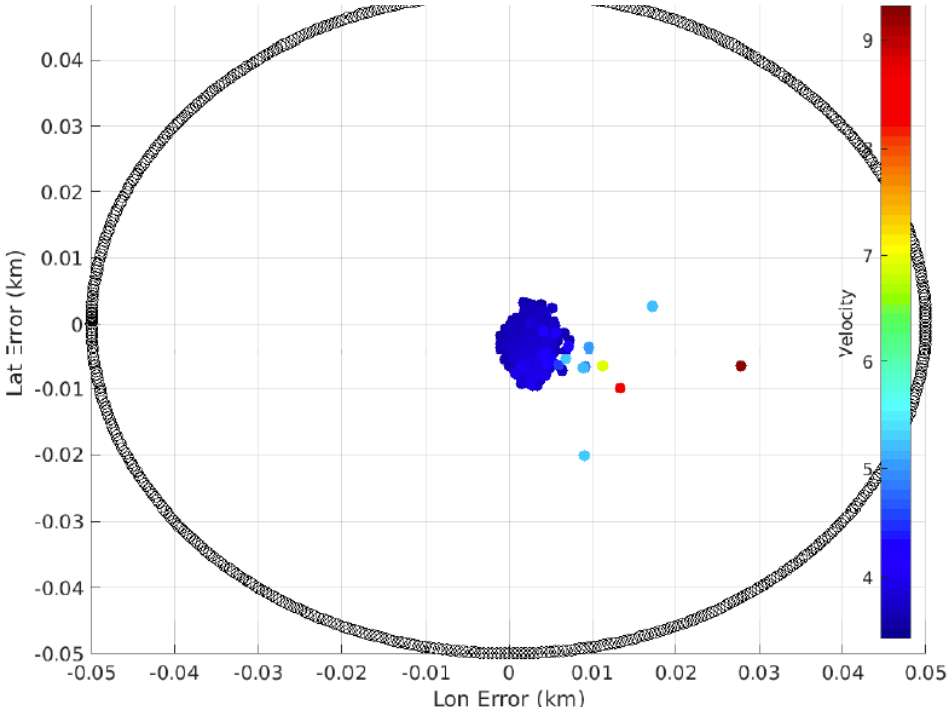

Figure 10. Miss Distance at Ground (0 m Altitude, k_r=12).

CONCLUSION

The results of 6DoF entry, descent, and landing trajectories using FNPEG and TAPDG have been presented for the mid-L/D vehicle CobraMRV 2908g. Nominal and off-nominal 6DoF entry cases have also been presented to illustrate the difficulties in attaining a 50 m radius footprint on the ground with low velocity. While all entry dispersed trajectories met the expected 3-5 km radius at the FNPEG termination energy, a small percentage of powered descent cases failed to meet the 50 m radius footprint on the ground for certain gains of k_r. A gain of 6, corresponding with E-guidance, is the preferred choice if TAPDG is used for future studies. The quartic equation for biasing t_{go} was necessary to achieve the targeting desired with TAPDG. More work will need to be done to assess the best TAPDG inputs to achieve the same level of success with a smarter PDI trigger with UPG and Augmented Apollo Powered Descent Guidance solution to assess how much more propellant savings are possible for this vehicle. The trajectory results imply that the control system approach of using aerosurfaces, main engines, and RCS jets provide an effective strategy for a human Mars MRV mission. These results achieve a major milestone in the EMC study.

Future work includes adding main engine throttle keep-out zones, improving gains used for RCS in powered descent to lessen propellant usage, and including a main engine aerodynamic database formulated by the aerodynamics team at the NASA Langley Research center. Modeling the usage of separate fuel and oxidizer tanks will be a useful future analysis to determine how much the CG may change in a real flight. Mitigation strategies, such as balancing the fuel rate consumption for

different tanks should be explored to ensure that the CG remains within controllable regimes. Challenge cases with high Y_{CG} and rolling moment uncertainties should be further investigated to determine higher sideslip TPS impacts, if any, and possible entry control algorithm mitigation strategies. Future wind tunnel tests of the flap effectiveness, RCS effectiveness, and SRP effectiveness will be vital in improving the uncertainties used in these simulations. Dynamic aerodynamic coefficients would be useful for increasing the fidelity of the current aerodynamic database (static coefficients), so any subscale flight tests could be useful in determining these coefficients and proving the G&C solution for hypersonic entry.

For these results, RCS is utilized to achieve the attitude commands in descent and landing, but future work should investigate using main engine differential throttling to help control attitude in a similar manner done in previous constant acceleration gravity turn studies.[9] Improvements in RCS propellant usage can be achieved with further analysis of the descent controls algorithm gains. Control actuator failure studies would help to mature the design to learn of other possible weakness of this approach. Future work would also include the aerocapture component of the EDL trajectory, where the deorbit from a 1-Sol vs. 5-Sol orbit is integrated with EDL. More information about MRV aerocapture performance statistics completed using the optimal solution from the Fully Numerical Predictor-corrector Aerocapture Guidance may be found in Reference 14. The work presented in this paper demonstrates that a feasible trajectory in landing a 20 mt payload to the surface of Mars within 50 m despite EDL dispersions is possible given the assumptions listed. A future analysis of these results with navigation errors will need to be completed to show how this accuracy degrades for a full Guidance, Navigation, and Control solution.

ACKNOWLEDGMENTS

The authors acknowledge all the individuals who contributed to this effort. We would like to extend gratitude to Ronald Sostaric, Phil Robinson, Joseph Garcia, Jeffrey Bowles, Daniel Matz, Kenneth Wong, Ellen Braden, Damien Calderon, Carlos Gaytan, Dave Kinney, Stan Bouslog, Holly Newton, Chuck Campbell, Alicia Cianciolo, Tara Polsgrove, and Francis Monahan. We really appreciate your guidance and value your expertise.

NOTATION

a_T	=	commanded thrust acceleration
C_A, C_Y, C_N	=	aerodynamic axial, side, and normal force coefficients
C_l, C_m, C_n	=	aerodynamic rolling, pitching, and yawing moment coefficients
g	=	acceleration due to gravity
h	=	altitude
$\dot{h}$	=	altitude rate
e	=	energy used in FNPEG
K	=	control system gain
L_{ref}	=	aerodynamic reference length
M	=	Mach
r	=	vehicle position
V	=	vehicle velocity
t	=	time
m	=	multiplier
s	=	range to target
p , q , r	=	inertial roll, pitch, and yaw rates
α	=	angle of attack
β	=	sideslip angle

ϕ	=	bank angle
$\bar{q}$	=	dynamic pressure
S	=	aerodynamic reference area
I	=	inertia
h_0	=	altitude at the start of the gravity turn
V_0	=	velocity at the start of the gravity turn
δ_r	=	rudder deflection
δ_e	=	elevon deflection
γ	=	flight path angle
μ	=	NED to body frame roll angle
ω	=	frequency
τ	=	torque
ξ	=	damping ratio
k_r	=	TAPDG trajectory shaping gain
U^a	=	aerodynamic coefficient uncertainty delta
U^m	=	aerodynamic coefficient uncertainty multiplier

REFERENCES

[1] Mendeck, G. and Craig, L., "Mars Science Laboratory Entry Guidance."

[2] Bihari, B. and Tigges, M., "Orion Capsule Handling Qualities for Atmospheric Entry," AIAA Guidance, Navigation, and Control Conference. Portland, Oregon.

[3] Martin-Mur, T. and Kruizinga, G., "Mars Science Laboratory Navigation Results."

[4] Cerimele, C., Robertson, E., Sostaric, R. (editor), Garcia, J., "A Rigid, Mid-Lift-to-Drag Ratio Approach to Human Mars Entry, Descent, and Landing," AIAA SciTech 2017, Grapevine, TX, Jan. 2017.

[5] Lu, P. "Augmented Apollo Powered Descent Guidance," In press, Journal of Guidance, Control, and Dynamics.

[6] Lu, P., "Entry Guidance: A Unified Method," Journal of Guidance, Control, and Dynamics, Vol. 37, No. 3 (2014), pp. 713-728.

[7] Lu, P., "Predictor-Corrector Entry Guidance for Low-Lifting Vehicles," Journal of Guidance, Control, and Dynamics, Vol. 31, No. 4 (2008), pp. 1067-1075.

[8] Johnson, B., Cerimele, C., Stachowiak, S., Sostaric, R., Matz, D., Lu, P., "Mid-Lift-to-Drag Ratio Rigid Vehicle Control System and Simulation for Human Mars Entry," AIAA, SciTech 2018, Kissimmee, Florida.

[9] Johnson, B., Braden, E., Sostaric, Cerimele, C., D., Lu, P., "Entry, Descent, and Landing Performance for a Mid-Lift-to-Drag ratio Vehicle at Mars," AAS, February 2018, Breckenridge, Colorado.

[10] Cherry, G. W., "A General, Explicit, Optimizing Guidance Law for Rocket-Propelled Spaceflight," AIAA Paper 64-638, 1964.

[11] Rogers, W. F., "Apollo Experience Report – Lunar Module Landing Gear Subsystem," Technical Note, Report No. NASA TN D-2850, Work Unit No 914-13-20-13-72, June 1972.

[12] Driels, M.R. and Shin, Y.S., "Determining the Number of Iterations for Monte Carlo Simulations of Weapon Effectiveness," Naval Postgraduate School, United States, 2004.

[13] D'Souza, C., "An Optimal Guidance Law for Planetary Landing," AIAA-97-3709, 1997.

[14] Matz, D., Lu, P., Mendeck, G., Sostaric, R., "Application of a Fully Numerical Guidance to Mars Aerocapture," AIAA-SciTech, DOI 10.2514/6.2017-1901, January 2017.